In-plane anisotropy of quantum elliptic heterostructures studied with symmetry-adapted Mathieu functions: an application to self-organized InAs quantum dots on InP

2003 J. Phys.: Condens. Matter 15 8737

(http://iopscience.iop.org/0953-8984/15/50/008)

INSTITUTE OF PHYSICS PUBLISHING JOURNAL OF PHYSICS: CONDENSED MATTER

J. Phys.: Condens. Matter **15** (2003) 8737–8752 PII: S0953-8984(03)70749-8

In-plane anisotropy of quantum elliptic heterostructures studied with symmetry-adapted Mathieu functions: an application to self-organized InAs quantum dots on InP

J Even, S Loualiche, P Miska and C Platz

Laboratoire d'Etude des Nanostructures à Semiconducteurs, INSA de Rennes, 20 Avenue des Buttes de Coesmes, CS 14315, F34043 Rennes Cedex, France

E-mail: jacky.even@insa-rennes.fr

Received 16 October 2003
Published 3 December 2003
Online at stacks.iop.org/JPhysCM/15/8737

Abstract

The problem of quantum-confined heterostructures with elliptic shape is studied with elliptic cylinder coordinates and a basis of symmetry-adapted Mathieu functions. The conventional effective mass Hamiltonian is written in two-dimensional and three-dimensional geometries. The problem is not separable in radial-like and angular-like coordinates. A variational method using a basis of symmetry-adapted Mathieu functions is proposed. Energy splitting, optical intersubband and interband transition spectra, and polarization effects are analysed. A calculation for self-organized InAs and InAs/InAlAs quantum dots on InP is performed. Various island shapes and morphologies are observed for such quantum dots, which may be important for potential applications in fibre optic telecommunication systems.

1. Introduction

Recent research developments have been devoted to quantum wires and quantum dots semiconductor heterostructures. They are promising as compared to semiconductor quantum wells for improving optoelectronic devices [1–3]. The theoretical study of the electronic properties of quantum wires (QWs) or quantum dots (QDs) can be performed with various theoretical schemes such as first-principles calculations, semi-empirical calculations (pseudopotential, tight binding) effective-mass or multiband kp approximations. The eight bands kp Hamiltonian together with the envelope function approximation has been used more or less as a standard model, in the particular case of QDs or QWs grown on GaAs or GaSb substrates [4–6]. One-band effective mass models have proved to be very useful in many cases for QDs grown either on GaAs or InP substrates [7–11]. In some cases, data from

characterization experiments are scarce. Strain, composition and shape must be carefully determined before applying complicated simulation methods. The shapes of the QWs or QDs are often known from experiments. Effective mass calculations for highly symmetric shapes (spherical QDs, cylindrical QWs or QDs) give the first indications on the influence of quantum confinement. It is interesting to study the effect of a simple shape deformation. This has been proposed for ellipsoidal QDs [12, 13] or elliptic cylindrical QWs and QDs [14, 15]. Optical anisotropy and polarization effects have been studied for ellipsoidal QDs [13].

In this paper, we will focus on the use of elliptic cylindrical coordinates [16]. Mathieu [17] studied elliptic geometry and introduced the so-called special Mathieu functions. These functions are the solutions of the Helmholtz equation, which is separable when using elliptic cylindrical coordinates [18–20]. They may be computed using the Matlab commercial mathematical software package[1]. Various problems may be conveniently treated with the elliptic cylindrical coordinates and Mathieu functions [18, 19, 21–25]. Among these problems, the oscillations of an elliptic membrane or the resonances of an elliptic cavity are closely related to the problem of studying the electronic properties of a heterostructure with an infinite potential barrier at the boundary [14, 18, 24, 25]. In the case of a finite potential barrier, it has been shown [15], contrary to a first assertion [14], that the problem is not separable in elliptic cylindrical coordinates. In this work, we propose a variational method using symmetry-adapted Mathieu functions and a simple one-band Hamiltonian in order to describe self-organized InAs and InAs/InAlAs QDs on InP. In that case, island shape may be important for long wavelength laser applications [26–32].

2. Geometrical descriptions of the quantum wires or dots

2.1. Elliptic cylindrical coordinates

The elliptic cylindrical set of coordinates ($0 \leqslant u \leqslant \infty$ and $0 \leqslant v \leqslant 2\pi$) is defined by a transformation of Cartesian coordinates (x, y) (see figure 1):

$$x = a\cosh(u)\cos(v)$$
$$y = a\sinh(u)\sin(v)$$
$$z = z.$$

An elliptic cylinder ($u = U$) is a coordinate surface ($\frac{x^2}{A^2} + \frac{y^2}{B^2} = 1$, where $A = a\cosh(U)$ and $B = a\sinh(U)$) represented in figures 1 and 2. Hyperbolic cylinders ($v = V$) are a second kind of coordinate surfaces (figure 1, dotted curves). Elliptic cylinders can be associated with a physical boundary. This set of coordinates has been used to model a variety of physical problems ranging from acoustics to fluid mechanics or electromagnetism [18, 19, 21–25]. Electronic states of heterostructures (QWs or QDs) can also be studied [14, 15]. If the boundary around the confined domain is defined by $u = U$, the elliptic surface is set equal to the surface of the reference circle $S = \pi R^2 = \pi AB$.

The eccentricity of the confined domain is $e = (1 - \frac{B^2}{A^2})^{1/2}$. Once the eccentricity and the surface of the confined domain are chosen, the a parameter defining the metric is fixed. The same procedure is used if the confined domain is enclosed in an external domain with a boundary $u = U_{\text{ext}}$ and $S_{\text{ext}} = \pi R_{\text{ext}}^2 = \pi A_{\text{ext}} B_{\text{ext}}$ (see figure 1). We may notice that the eccentricity of the boundary e_{ext} is smaller than the eccentricity of the confined domain e.

For the same reason, it is also interesting to use circular cylindrical coordinates when the boundary of the heterostructure is circular ($r = R$). In that case ($0 \leqslant r \leqslant \infty$ and $0 \leqslant \theta \leqslant 2\pi$)

$$x = r\cos(\theta)$$

[1] Matlab, Version 6.0, (The MathWorks Inc., Natick 2000).

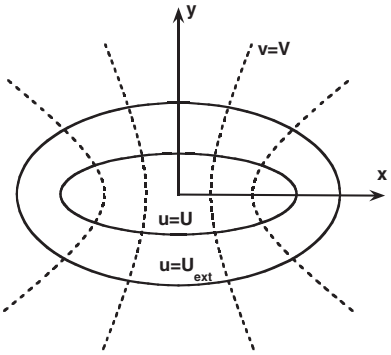

Figure 1. The elliptic cylindrical set of coordinates. The coordinate surfaces are projected on the xy-plane. Elliptic cylinders ($u = U$) are represented by full curves. Hyperbolic cylinders ($v = V$) are represented by dotted curves. A confined elliptical domain $u = U$ is enclosed in an exterior elliptical domain $u = U_{\text{ext}}$. U_{ext} is a boundary limit fixed by the targeted accuracy of the computed results. The eccentricity of the exterior domain is smaller.

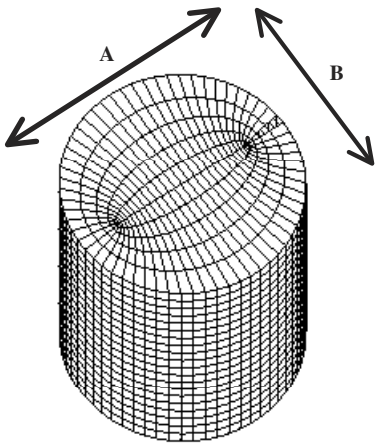

Figure 2. Quantum wires or quantum dots problems may be studied with elliptic cylindrical coordinates. Such 3D geometrical objects are obtained by extending the 2D geometrical objects (ellipses) along the z-axis. A and B are dimensions along the axes of the ellipse.

$$y = r\sin(\theta)$$
$$z = z.$$

The circular cylindrical set of coordinates will be a reference set in our model corresponding to an eccentricity equal to zero.

2.2. Symmetry properties

The corresponding symmetry of a circular heterostructure (with eccentricity equal to zero) is either $C_{\infty v}$ or $D_{\infty h}$. In the last case, a symmetry plane is added perpendicular to the rotation axis. $D_{\infty h}$ is the direct product of $C_{\infty v}$ and C_i; $C_{\infty v}$ is related to symmetries in the xy-plane and C_i to symmetries along the z-axis. The symmetry group is either C_{2v} or D_{2h} if the eccentricity is different from zero. When comparing the circular and elliptic sets of coordinates, we will only use the irreducible representations (IRs) of the $C_{\infty v}$ and C_{2v} symmetry groups (see table 1).

$C_{\infty v}$	C_{2v}
S	A_1
S^-	A_2
P	B_1+B_2
D	A_1+A_2
F	B_1+B_2
G	A_1+A_2

Figure 3. Relations between the IRs of the $C_{\infty v}$ symmetry group and the IRs of the C_{2v} symmetry group.

Table 1. Character table of the IRs of the C_{2v} symmetry group.

	A1	A2	B1	B2
E	1	1	1	1
C2	1	1	−1	−1
σ_{xz}	1	−1	−1	1
σ_{yz}	1	−1	1	−1

In order to study the effect of an elliptical shape versus a circular one, it is important to know the relations between the IRs of the $C_{\infty v}$ group and the IRs of the C_{2v} group (see figure 3). There is an infinite number of IRs for the $C_{\infty v}$ group. The dimensionalities of S and S^- are equal to 1 whereas for all the others (P, D, F, G ...) it is equal to 2. There are only four IRs for the C_{2v} group: A1, A2, B1 and B2 (see table 1). The IR S of the $C_{\infty v}$ group is related to the A1 IR of the C_{2v} symmetry group (see figure 3). The IR S^- of the $C_{\infty v}$ group is related to the A2 IR of the C_{2v} symmetry group. The IRs P, D, F, G ... of the $C_{\infty v}$ group are split between the IRs (A1, A2) or (B1, B2) of the C_{2v} symmetry group.

When a one-band envelope function Hamiltonian is considered, the symmetry analysis of the geometry is still correct if the potential and the in-plane effective mass depend only on r for the circular case and on u for the elliptic case. For the electronic wavefunctions [7–9], the quantum number n, which originates from the angular part of the solution $e^{in\theta}$, is used with the labels S ($n = 0$), P ($n = 1$), D ($n = 2$) ... for the $C_{\infty v}$ group. For a multi-band Hamiltonian, this is not correct since the symmetry properties of the Bloch functions must be taken into account. The axial approximation is useful in that case for the circular cylindrical case [6].

3. Effective mass Hamiltonians using elliptic cylindrical coordinates

3.1. The quantum wire problem

3.1.1. One-band 2D Hamiltonians. We will first recall some already known results for the circular case before analysing the elliptic case. The circular cylindrical metric is defined by three coefficients: $h_{11} = 1$, $h_{22} = r$ and $h_{33} = 1$ [16]. The usual symmetrization of the expression $\vec{p}^2/2m(\vec{r})$ yields the hermetic Hamiltonian $\hat{H} = \frac{1}{2}\hat{p}\frac{1}{m(\vec{r})}\hat{p} + V(\vec{r})$ with $\hat{p} = -i\hbar\vec{\nabla}$ [33, 34]. The effective mass m^r does not depend on θ [7]. The kinetic part of the Hamiltonian is then defined by

$$\hat{H}_c\Psi = -\frac{i\hbar}{2}\vec{\nabla}\vec{F} = -\frac{\hbar^2}{2}\left[\frac{1}{r}\frac{\partial}{\partial r}\frac{r}{m^r_{(r)}}\frac{\partial}{\partial r} + \frac{1}{m^r_{(r)}}\frac{\partial^2}{r^2\partial\theta^2}\right]\Psi \tag{1}$$

where

$$\vec{F} = \frac{1}{m(\vec{r})}\hat{p}\Psi \qquad \text{is} \qquad \vec{F} = -\mathrm{i}\hbar \begin{vmatrix} \frac{1}{m^r}\frac{\partial \Psi}{\partial r} \\ \frac{1}{m^r}\frac{1}{r}\frac{\partial \Psi}{\partial \theta} \end{vmatrix}.$$

This approach may be extended to the elliptic cylindrical case. The elliptic cylindrical metric is defined by three coefficients: $h_{11} = h_{22} = a(\cosh(u)^2 - \cos(v)^2)^{1/2}$ and $h_{33} = 1$ [16]. The effective mass m^u does not depend on v.

$$H_c\Psi = -\frac{\mathrm{i}\hbar}{2}\vec{\nabla}\vec{F} = -\frac{\hbar^2}{2a^2(\cosh(u)^2 - \cos(v)^2)}\left[\frac{\partial}{\partial u}\frac{1}{m^u_{(u)}}\frac{\partial}{\partial u} + \frac{1}{m^u_{(u)}}\frac{\partial^2}{\partial v^2}\right]\Psi \tag{2}$$

where

$$\vec{F} = \frac{1}{m(\vec{r})}\hat{p}\Psi \qquad \text{is} \qquad \vec{F} = -\mathrm{i}\hbar \begin{vmatrix} \frac{1}{m^u}\frac{1}{a(\cosh(u)^2-\cos(v)^2)^{1/2}}\frac{\partial \Psi}{\partial u} \\ \frac{1}{m^u}\frac{1}{a(\cosh(u)^2-\cos(v)^2)^{1/2}}\frac{\partial \Psi}{\partial v} \end{vmatrix}.$$

3.1.2. The separability of 2D Hamiltonians. The 2D Hamiltonian in circular coordinates is always separable in r and θ providing that the potential and the effective mass only depend on r ($\Psi(r,\theta) = f(r)g(\theta)$ where $g(\theta) = \mathrm{e}^{\mathrm{i}n\vartheta}$):

$$-\frac{\hbar^2}{2}\left[\frac{1}{r}\frac{\partial}{\partial r}\frac{r}{m^r_{(r)}}\frac{\partial \Psi}{\partial r} + \frac{1}{m^r_{(r)}}\frac{\partial^2\Psi}{r^2\partial\,\theta^2}\right] + V(r)\Psi = E\Psi \tag{3}$$

$$C = \frac{-1}{g}\frac{\partial^2 g}{\partial\theta^2} = n^2. \tag{4}$$

The separation constant C is equal to n^2 ($n = 0, 1, 2, 3 \ldots$) because the function g is periodic. In the infinite potential well case, the solutions of the Schrödinger equation are Bessel functions $\Psi^n_l(r,\theta) = N^n_l J_n(k^n_l \frac{r}{R})\mathrm{e}^{\mathrm{i}n\theta}$ where l corresponds to the lth zero of the radial function and R is the radius of the confined domain. N^n_l is a normalization constant. The energies are $E_{l,n} = (k^n_l)^2 E_\infty$ where $E_\infty = \hbar^2/(2m^r R^2)$.

The two-dimensional Hamiltonian in elliptic coordinates is written by adding a confining potential $V(u)$ to the kinetic part (equation 2). Figure 4 is a representation of a confining potential $V(u)$ with a step-like variation. The potential is set equal to zero inside the QW and V outside the QW. Confined states have energy values between zero and V. In the infinite potential well case, the Schrödinger equation reduces to the well-known Helmholtz equation; the solution is given in [14, 18]. The wavefunction is $\Psi(u,v) = f(u,k)g(v,k)$ ($0 \leqslant u \leqslant U$ and $0 \leqslant v \leqslant 2\pi$) and the problem is separable in u and y:

$$\frac{\mathrm{d}^2 f}{\mathrm{d}u^2} + \left[\frac{k^2}{2}\cosh(2u) - c\right]f = 0 \qquad \text{and} \qquad \frac{\mathrm{d}^2 g}{\mathrm{d}v^2} + \left[-\frac{k^2}{2}\cos(2v) + c\right]g = 0 \tag{5}$$

where c is the separation constant and k is related to the reduced energy $E = k^2 E_\infty$ with $E_\infty = \hbar^2/(2m^u a^2)$. The periodicity $0 \leqslant v \leqslant 2\pi$ yields a first relation $c(k)$ and a second relation $c(k)$ is given by $f(U) = 0$. The symmetry is related to the behaviour of the angular-like Mathieu $g(v)$ functions [18]: the A1 IR corresponds to $ce_n(k,v)$ with n even ($n = 0, 2, 4 \ldots$), B1 to $ce_n(k,v)$ with n odd ($n = 1, 3, 5 \ldots$), A2 to $se_n(k,v)$ with n even ($n = 2, 4 \ldots$) and B2 to $se_n(k,v)$ with n odd ($n = 1, 3, 5 \ldots$). Each solution for a given IR is then $\Psi^n_l(u,v) = f^n_l(u,k^n_l)g_n(v,k^n_l)$, where l corresponds to the lth zero of the radial-like Mathieu function [18]. The (kinetic) confined energies are $E_{l,n} = (k^n_l)^2 E_\infty$.

We show now that the energy is never separable in u and v if the potential or the effective mass depends on u, in contradiction to [14]. In the general case, if one tries

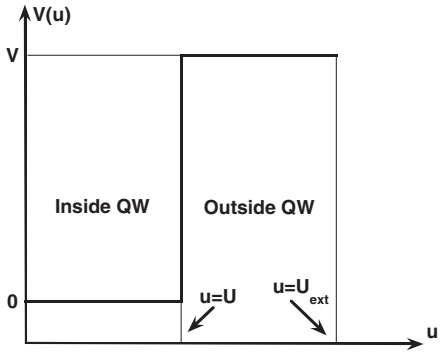

Figure 4. The evolution of the confining potential as a function of the radial-like coordinate u. The potential is set equal to zero inside the quantum wire and V outside the quantum wire.

$\Psi(u, v) = f(u)g(v)$, the Hamiltonian equation

$$-\frac{\hbar^2}{2a(\cosh(u)^2 - \cos(v)^2)}\left[\frac{\partial}{\partial u}\frac{1}{m^u_{(u)}}\frac{\partial \Psi}{\partial u} + \frac{1}{m^u_{(u)}}\frac{\partial^2 \Psi}{\partial v^2}\right] + V(u)\Psi = E\Psi \qquad (6)$$

yields

$$\frac{m^u_{(u)}}{f}\frac{\partial}{\partial u}\frac{1}{m^u_{(u)}}\frac{\partial f}{\partial u} + \frac{2a^2 m^u_{(u)}}{\hbar^2}(E - V(u))(\cosh(u)^2 - \cos(v)^2) = \frac{-1}{g}\frac{\partial^2 g}{\partial v^2}. \qquad (7)$$

The term $(\cosh(u)^2 - \cos(v)^2)$, having a mixed u, v dependence, prevents the use of a separation constant between f and g. We must point out that even if one tries to make a variable separation in two domains as proposed in [14], the continuity relations between the domains could not be fulfilled as shown in [15]. It is indeed known from the literature for other problems [18] that interior or exterior problems can only be treated separately with this set of coordinates. Interior or exterior problems described by the Schrödinger equation given in this work cannot be treated by a single variable separation. The problem of finding the eigenfunctions must be solved by more elaborated methods: by making infinite expansions of the solution on both sides of the interface and matching these expansions for $u = U$ as proposed in [15], or by using a variational approach for the whole domain as proposed in what follows. The results of an infinite expansion of the solutions on both sides [15] have been compared to the results of an incorrect variable separation [14]. The same limiting eigenvalues are obtained for the circular case but not for the elliptical case associated to a finite potential barrier.

3.2. A variational calculation in 2D

3.2.1. The cylindrical reference case. Analytical results are obtained in the literature for the circular case using Bessel functions J in the confined domain and K outside (see, for example, [34]). The circular case is a reference for our study of the elliptic 2D case because we can also use a variational method with a basis of Bessel J functions in addition to the analytical method. The confinement potential is set equal to zero inside the circle and V outside. The surface of the circle is $S = \pi R^2$. Following [7], this circle is enclosed inside a circle of external boundary R_{ext} where the Bessel J functions are forced to vanish. Each basis function is then $\xi^n_l(r, \theta) = N^n_l J_n(k^n_l \frac{r}{R_{\text{ext}}})e^{in\theta}$, where l corresponds to the lth zero of the

radial function. N_l^n is a normalization constant. The basis functions are orthonormalized. The Hamiltonian matrix is block diagonalized for each n value (for each IR of the $C_{\infty v}$ group). If the effective mass is the same in both domains, the kinetic part of the Hamiltonian matrix is diagonal:

$$H^c_{l,n;l',n'} = E_{l,n}\delta_{nn'}\delta_{ll'} = E_\infty (k_l^n)^2 \delta_{nn'}\delta_{ll'} \qquad \text{with } E_\infty = \frac{\hbar^2}{2m^r R_{\text{ext}}^2}. \tag{8}$$

The potential part of the Hamiltonian is defined by

$$H^v_{l,n;l',n'} = 2\pi V \int_{r=R}^{R_{\text{ext}}} N_{l'}^{n'} J_{n'}\left(k_{l'}^{n'}\frac{r}{R_{\text{ext}}}\right) N_l^n J_n\left(k_l^n \frac{r}{R_{\text{ext}}}\right) \mathrm{d}S\, \delta_{nn'}. \tag{9}$$

This part can also be put into a complete analytical form [7]. In order to limit the wavefunction expansion, it is interesting to define a kinetic energy cut-off E_{cut}. Only the basis functions with $E_{l,n} = E_\infty (k_l^n)^2 \leqslant E_{\text{cut}}$ are considered. For example, when the parameters are $m^r = 0.04\, m_0$, $V = 300$ meV, $R = 17.5$ nm and $R_{\text{ext}} = 35$ nm, the energy cut-off is $E_{\text{cut}} = 475$ meV when a numerical accuracy of the order of 1 meV is required for the ten lowest energy eigenvalues. The number of Bessel functions in the expansion is equal to about ten functions for $E_{\text{cut}} = 475$ meV. It is, finally, important to check that the value for R_{ext} is large enough so that the accuracy of the integral computations does not depend on this parameter.

3.2.2. Elliptical geometry. We propose a variational calculation based on a set of symmetry adapted Mathieu functions. The ellipse defining the confined domain is enclosed inside an ellipse of external boundary $u = U_{\text{ext}}$ where the Mathieu basis functions are forced to vanish (see figure 1). This is equivalent to the Helmholtz problem (see section 3.2). The k_l^n value depends both on l and on the chosen angular function n. Each basis function for a given IR is then $\xi_l^n(u,v) = f_l^n(u,k_l^n)g_n(v,k_l^n)$ and is orthonormalized by

$$\langle \xi_l^n(u,v) | \xi_{l'}^{n'}(u,v)\rangle = \int_{u=0}^{U_{\text{ext}}}\int_{v=0}^{2\pi} f_l^n(u,k_l^n) g_n(v,k_l^n) f_{l'}^{n'}(u,k_{l'}^{n'}) g_{n'}(v,k_{l'}^{n'})\,\mathrm{d}S = \delta_{nn'}\delta_{ll'}. \tag{10}$$

This is a general property of the eigenfunctions of the Liouville equation arising from the separation of the Helmholtz equation [18]. The area element is $\mathrm{d}S = a^2(\cosh^2(u) - \cos^2(v))\,\mathrm{d}u\,\mathrm{d}v$ [16]. The variational method may be applied for a given IR by decomposing the wavefunctions on the basis of the Mathieu functions: $\Psi(u,v) = \sum_{l,n} A_{l,n}\xi_l^n(u,v)$. The Hamiltonian matrix elements are $H_{l,n;l',n'} = \langle \xi_l^n(u,v)|H|\xi_{l'}^{n'}(u,v)\rangle$.

The matrix is block diagonalized in four blocks corresponding to the four IR. If the effective mass is the same in both domains, the kinetic part of the Hamiltonian matrix is diagonal:

$$H^c_{l,n;l',n'} = E_\infty (k_l^n)^2 \delta_{nn'}\delta_{ll'} \qquad \text{with } E_\infty = \frac{\hbar^2}{2m^u a^2}. \tag{11}$$

The potential part of the Hamiltonian matrix is given by the elements

$$H^v_{l,n;l',n'} = V \int_{u=U}^{U_{\text{ext}}}\int_{v=0}^{2\pi} f_l^n(u,k_l^n) g_n(v,k_l^n) f_{l'}^{n'}(u,k_{l'}^{n'}) g_{n'}(v,k_{l'}^{n'})\,\mathrm{d}S. \tag{12}$$

In order to make a comparison with the circular case, we choose the same effective mass and the same confinement potential. The kinetic energy cut-off calculated for the circular case is applied to the basis of Mathieu functions:

$$E_{l,n} = E_\infty (k_l^n)^2 \leqslant E_{\text{cut}}. \tag{13}$$

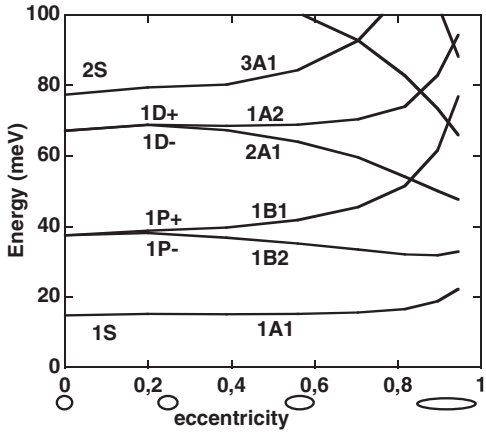

Figure 5. The evolution of the electronic energies as a function of the eccentricity in the case when $V = 300$ meV and $m = 0.04\ m_0$. The states are labelled according to the IRs of the C_{2v} or $C_{\infty v}$ symmetry groups.

3.3. The influence of in-plane anisotropy on the properties of 2D heterostructures

3.3.1. Calculations of 2D electronic states and wavefunctions. In order to analyse the influence of in-plane anisotropy, we have decided to study a model case. The surface is set equal to the surface of the reference circle ($m^r = 0.04\ m_0$, $V = 300$ meV, $R = 17.5$ nm). Figure 5 represents the evolution of the energies as a function of the eccentricity. The labels defined for the circular case (S, P, D) are indicated together with the labels defined for the elliptic case (A1, A2, B1, B2). The 1A1(1S) state is the ground state. The degenerate 1D state ($n = 2$) is split into a 1A2($1D^+$) state and a 2A1($1D^-$) state. The 2A1($1D^-$) state has an energy between those of the 1A1(1S) and 3A1(2S) states. These three states belong to the same IR(A1) in the elliptic case. The degenerate 1P state ($n = 1$) is split into the 1B1($1P^+$) state and the 1B2($1P^-$) state. No mixing of the P states with the S states is possible. Various crossings are observed. The 2A1($1D^-$) state crosses the 1B1($1P^+$) state for an eccentricity equal to about 0.82. This crossing is the most important one among the lowest energies excited states. It corresponds to $A = 23.1$ nm and $B = 13.2$ nm ($R = 17.5$ nm) and thus a ratio $A/B = 1.75$, which is in good agreement with the same ratio calculated from figure 1 in [15]. Figure 5 in this work presents in addition the result of a symmetry analysis. It shows that no level anticrossing is expected when the eccentricity is increased. Levels crossings have also been analysed for ellipsoidal quantum dots [13].

Figure 6 shows the electronic wavefunctions of the lowest energy states for the four IRs of the C_{2v} group compared with the same electronic wavefunctions in the circular case. The eccentricity of the confined domain is equal to 0, 0.39 and 0.90 respectively. The first A1 state labelled 1A1 is the ground state. The first B1 and B2 functions (1B1 and 1B2) correspond to the degenerate 1P states oriented along the small or long axes of the ellipse. They have a vectorial symmetry. The 1A2 and 2A1 states correspond to the degenerate 1D states.

Figure 7 is a representation of two wavefunctions along the x-axis. The eccentricity of the confined domain is equal to 0 (full curves) and 0.9 (dotted curves). The variation of the 1A1(1S) ground state wavefunction along the x-axis is similar in the two cases because the derivatives of the functions must vanish for $x = 0$ (see figure 7(a)). The 2A1($1D^-$) wavefunction shape changes on increasing the eccentricity. A change in the boundary conditions is associated with the change of symmetry groups. For the $1D^-$ wavefunction, the function and the derivative of

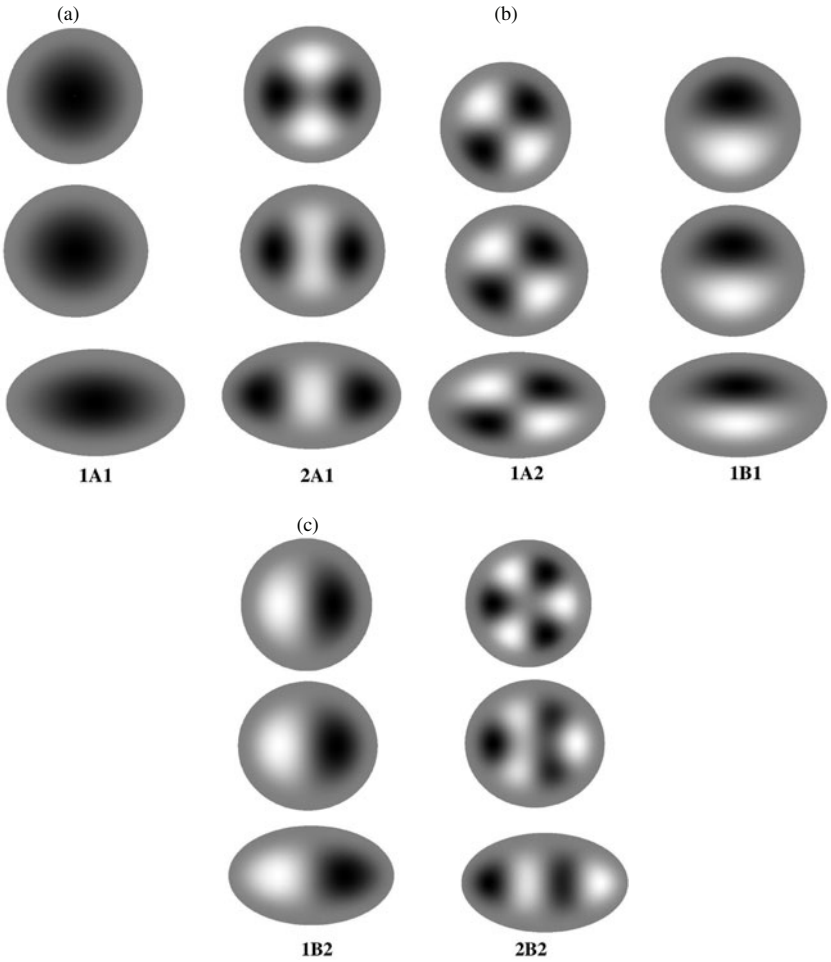

Figure 6. (a) The first A1 electronic wavefunctions. The 1A1 and 2A1 functions are represented for an eccentricity equal to 0 (circular case), 0.39 and 0.90 in the case when $V = 300$ meV and $m = 0.04\ m_0$. (b) The first A2 (left) and B1 (right) electronic wavefunctions represented for an eccentricity equal to 0 (circular case), 0.39 and 0.90. The first 1A2 function (left) corresponds to the $1D^-$ function The 1B1 function (right) corresponds to the $1P^+$ function. (c) B2 electronic wavefunctions represented for an eccentricity equal to 0 (circular case), 0.39 and 0.90. The 1B2 function (left) corresponds to the $1P^-$ function.

the functions must vanish for $x = 0$, whereas for the 2A1 wavefunction, only the derivative of the functions must vanish for $x = 0$ (figure 7(b)).

3.3.2. Optical interband transitions. The electron–hole optical oscillator strengths for interband transitions are proportional to the integral $I_{\mathrm{eh}} = \langle \Psi_{\mathrm{e}}(u, v)\Psi_{\mathrm{h}}(u, v)\rangle$ where e stands for electrons and h for holes. It can be easily calculated using the coefficients of the Mathieu function expansions $I_{\mathrm{eh}} = \sum_{l,n} A^{\mathrm{e}}_{l,n} A^{\mathrm{h}}_{l,n}$. We have simulated such transitions by performing a first calculation with $m = 0.04\, m_0$, $V = 300$ meV for electrons and a second with $m = 0.4\, m_0$, $V = 300$ meV for holes. Figure 8 is a simplified representation of the optical interband spectra for an eccentricity of the confined domain equal to 0 (full curves) and 0.82 (dotted curves). The value $e = 0.82$ corresponds to $A = 23.1$ nm and $B = 13.2$ nm ($R = 17.5$ nm). Some

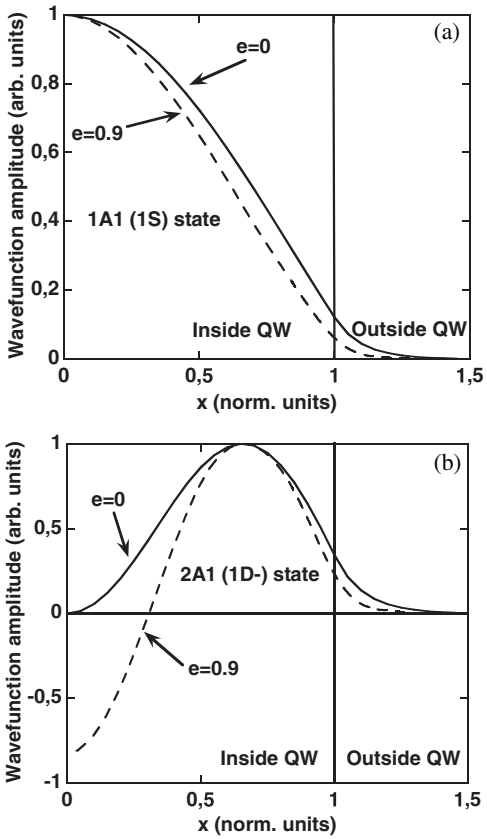

Figure 7. (a) The evolution of the 1A1(1S) wavefunction amplitude as a function of the normalized radial coordinate along the x-axis for an eccentricity equal to 0 and 0.9. The boundary of the quantum dot corresponds to $x = 1$. (b) The evolution of the 2A1($1D^-$) wavefunction amplitude as a function of the normalized radial coordinate along the x-axis for an eccentricity equal to 0 (a) or 0.9 (b). The boundary of the quantum dot corresponds to $x = 1$. The derivative of the wavefunction $1D^-$ and the wavefunction itself must vanish at $x = 0$ whereas only the derivative of the 2A1 wavefunction must vanish at $x = 0$.

transitions such as the 1A1(1S)–2A1($1D^-$) one are forbidden in the circular case and allowed in the elliptic case but remain weak. The transitions corresponding to the same electron or hole state are labelled on figure 8 (for example, 1S for 1S–1S or 1A1 for 1A1–1A1 transitions). The splitting of the 1P and 1D electron and hole states gives rise to a splitting of the interband 1P and 1D transitions. The 1P and 1D interband transitions are split respectively into 1B2 and 1B1 transitions, and 2A1 and 1A2 transitions. The value of the eccentricity $e = 0.82$ was chosen because the 2A1($1D^-$) state and the 1B1($1P^+$) state are degenerate (see figure 5). The 2A1 and 1B1 electron and hole states yield optical interband transitions at almost the same energy (figure 8). This shows that the interpretation of optical interband spectra may be difficult for a quantum heterostructure with an elliptical symmetry. It should be combined if possible with a study of optical intersubband transitions, as shown in what follows.

3.3.3. Optical intersubband transitions. General selection rules may be derived for the optical intersubband transitions between electronic states. Polarization effects may also be

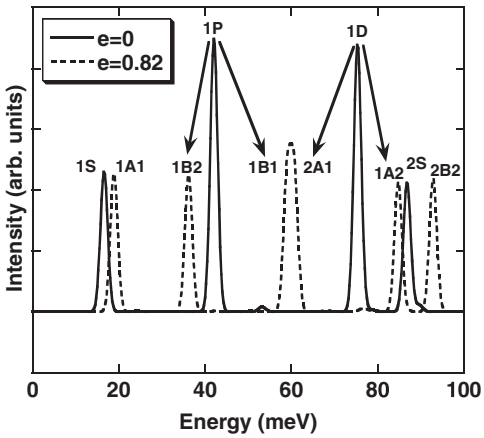

Figure 8. Simulations of the interband optical spectra in the circular case (full curves) and in the elliptical case (dotted curves, eccentricity equal to 0.82). The energy axis represents the confined energies for which the gap energy is added to obtain transition energies. The optical transitions between different electron and hole states remain weak. The labels for the optical transitions correspond to transitions between the same electron and hole states (for example 1S is the 1S–1S interband optical transition). The splittings of 1P and 1D optical transitions are represented by the arrows.

predicted. The optical oscillator strengths for these transitions are proportional to the dipolar lengths, the integrals $I_{\mathrm{e1e2}} = \langle \Psi_{\mathrm{e1}}(u,v)|x|\Psi_{\mathrm{e2}}(u,v)\rangle$ and $I_{\mathrm{e1e2}} = \langle \Psi_{\mathrm{e1}}(u,v)|y|\Psi_{\mathrm{e2}}(u,v)\rangle$ for light polarized along the x- and y-axes respectively. For light polarized along the x-axis, the transitions may be observed either between A1 and B2 states or between A2 and B1 states. For light polarized along the y-axis, selection rules indicate that the transitions may be observed either between A1 and B1 states or between A2 and B2 states. In the circular case, the 1S–1P$^+$ and 1S–1P$^-$ transitions correspond to the same energy and oscillator strength. This is not true for the elliptic case. Optical oscillator strengths for an A1–B1 transition are calculated by computing first the integrals between the basis functions $I_{l,n,\mathrm{A1};l',n',\mathrm{B1}} = \langle \xi^n_{l,\mathrm{A1}}(u,v)|a\cosh(u)\cos(v)|\xi^{n'}_{l',\mathrm{B1}}(u,v)\rangle$, and second the sum $I_{\mathrm{A1-B1}} = \sum_{l,n}\sum_{l',n'} A_{\mathrm{A1},l,n}A_{\mathrm{B1},l',n'}I_{l,n,\mathrm{A1};l',n',\mathrm{B1}}$. For experimental studies, n-doped samples are often used [11]. Optical intersubband transitions are then only observed between the electronic ground state and some electronic excited states. In our theoretical study, it corresponds to transitions between the 1A1 ground state and B2 (polarization along the x-axis) or B1 (polarization along the y-axis) states. Figure 9 represents the polarized optical absorption spectra in the elliptic case (the eccentricity of the confined domain is equal to 0.8). The positions, intensities and polarizations of the transitions are a function of the eccentricity. The splitting of the 1P electron state corresponds to a splitting of the 1S–1P intersubband transitions. This may be studied by optical intersubband spectroscopy [11]. It confirms that by realizing anisotropic systems, polarization-dependent processes can be obtained. It was shown indeed that the more the ellipsoidal dot geometry is different from the spherical one, the more anisotropic is its response to polarized radiation [13]. The same result is found here.

3.4. The quantum dot problem

3.4.1. The one-band 3D Hamiltonian. The effective mass is anisotropic and the two mass components m^r and m^z do not depend on θ [7]. The kinetic part of the Hamiltonian for

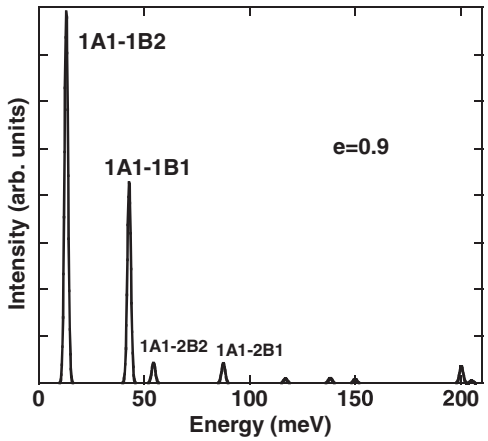

Figure 9. Simulations of the electronic intersubband optical spectrum in the elliptical case (eccentricity equal to 0.9) assuming that the 1A1 ground state is the only state populated by the n-doping of the sample. 1A1–B2 transitions are optical transitions with polarization along the x-axis whereas 1A1–B1 transitions are optical transitions with polarization along the y-axis. The lowest transition energies are 1A1–1B2 and 1A1–B1 for the two polarizations respectively. The polarizations, intensities and positions of the transitions depend on the eccentricity.

cylindrical coordinates is then defined by

$$H_c\Psi = -\frac{\mathrm{i}\hbar}{2}\vec{\nabla}\vec{F} = -\frac{\hbar^2}{2}\left[\frac{1}{r}\frac{\partial}{\partial r}\frac{r}{m^r_{(r,z)}}\frac{\partial}{\partial r} + \frac{1}{m^r_{(r,z)}}\frac{\partial^2}{r^2\,\partial\theta^2} + \frac{\partial}{\partial z}\frac{1}{m^z_{(r,z)}}\frac{\partial}{\partial z}\right]\Psi. \tag{14}$$

Using the same procedure for elliptic coordinates, it is straightforward to obtain

$$H_c\Psi = -\frac{\mathrm{i}\hbar}{2}\vec{\nabla}\vec{F} = -\frac{\hbar^2}{2a^2(\cosh(u)^2-\cos(v)^2)}\left[\frac{\partial}{\partial u}\frac{1}{m^u_{(u,z)}}\frac{\partial}{\partial u} + \frac{1}{m^u_{(u,z)}}\frac{\partial^2}{\partial v^2} + \frac{\partial}{\partial z}\frac{1}{m^z_{(u,z)}}\frac{\partial}{\partial z}\right]\Psi. \tag{15}$$

3.4.2. The separability of 3D Hamiltonians. The 3D Hamiltonian in circular cylindrical coordinates is separable in (r, z) and θ only, because the potential $V(r, z)$ and the effective masses have a mixed dependence on r and $z(\Psi(r, \theta, z) = f(r, z)g(\theta))$ [7]. This result is confirmed by carefully inspecting the boundary conditions. The 3D Hamiltonian in elliptic cylindrical coordinates is not separable in u, z and v even if the potential and the effective masses depend only on u and z.

3.4.3. Variational calculation in 3D. A variational approach with symmetry-adapted Bessel and sinus functions was proposed in [7] for circular cylindrical coordinates. Our variational approach in 3D is an extension of the one in 2D where sinus basis functions are used together with symmetry-adapted Mathieu functions. The sinus basis functions are forced to vanish on the external boundary $z = \pm L/2$, where L is the thickness of the external domain.

4. The application to self-organized InAs quantum dots on InP

4.1. Introduction

Most of the research on III–V QDs has been devoted to InAs or (In, Ga)As QDs grown on GaAs substrates. However, lasers operating at the optical telecommunication wavelength of 1.55 μm have not been achieved using such dots. QDs on InP substrates may emit in this range. This subject has attracted recently the attention of our laboratory and of many other scientists [10, 11, 26–30, 32, 35–39].

The lattice mismatch in the InAs/InP system is however much smaller than the one in the InAs/GaAs system. It complicates the reproducible formation of nanometer-sized islands. The island nucleation and growth are then strongly dependent on the experimental conditions. Weak changes of the growth conditions result in large changes of the nanostructures characteristics. Isotropic QDs have been obtained by using an InP(113)B substrate [10, 26, 28, 30, 32, 35, 41]. Various island shapes and morphologies are observed with an InP(100) substrate, ranging from elongated QDs (quantum dashes or 'QWs') to almost isotropic QDs [36]. Moreover, the determination of the morphology of the islands by experimental techniques such as atomic force microscopy (AFM) is difficult. Islands with and without a capping layer have different dimensions because the As/P exchange reaction is important [35]. High-resolution electron microscopy transmission (TEM) measurements yield more accurate geometrical descriptions of the islands.

The linewidth enhancement factor (LEF) and chirp are key parameters for lasers operating at telecommunication wavelengths [31, 40]. The LEF can be made zero only if the absorption spectrum decreases strongly above the laser frequency [40]. This can be achieved if the separation between the ground state transition (GS) and the first excited state transition (ES) is greater than the broadening. This condition is difficult to obtain for InAs QDs grown on InP; an additional difficulty is that at the same time, GS must correspond to the optical telecommunication wavelength of 1.55 μm. The difference between GS and ES has been measured directly for almost isotropic (113)B QDs by optical spectroscopy [41]. It is equal to about 50 meV and is of the order of the inhomogeneous broadening. This result has been confirmed by laser emission study [26, 28, 30]. The anisotropy of InAs(100) islands has an influence on the GS–ES separation. A reduced GS–ES separation is obtained when increasing the geometrical anisotropy, as shown in section 3.3.2 (see figure 8). Indeed a smaller GS–ES separation of 32 meV has been measured for lasers with an active layer containing InAs quantum dashes on InP(100) substrate [27]. This is probably the reason why low chirp has been observed only for InAs QD grown on (113)B substrate [32].

In what follows, we will consider two examples of InAs quantum islands grown on InP(100). For our simulations, we will use the variational calculation of the one-band 3D Hamiltonian (see section 3.4) together with some material parameters from [10, 11, 41]. In these works, a reasonable agreement was found between experimental and theoretical results for the optical transitions, using an effective mass approach and a simplified description of the strains and geometry of the dots.

4.2. The application to self-organized InAs/InAlAs QDs on InP substrate

We first apply our model to the case of self-organized InAs/InAlAs QDs on InP substrate [11]. The electronic energies were fitted in this paper for a well size of 2.92 nm (thickness), 150 nm and 17.8 nm (the dimensions of the wire along the $[1\bar{1}0]$ and [110] directions which are crystal denominations of, respectively, the x- and y-directions). These dimensions are in good agreement with high-resolution electron microscopy transmission (TEM) measurements. The

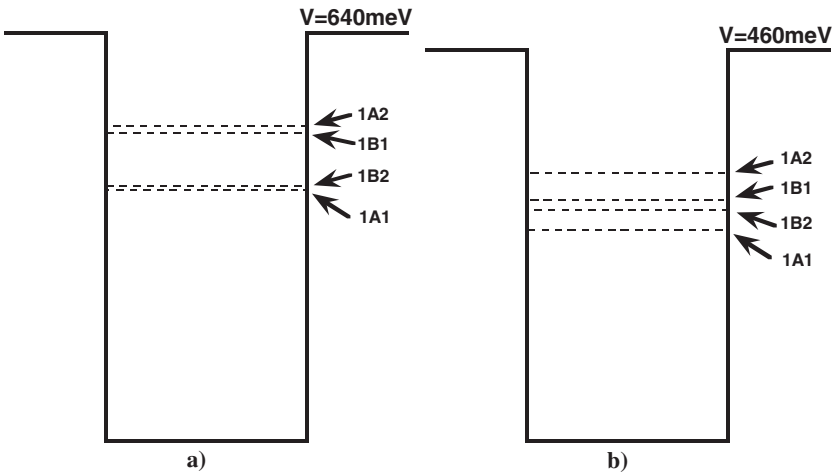

Figure 10. (a) The electronic spectrum for an elliptic InAs/InAlAs QD with thickness 2.92 nm, and long and short axes 150 and 17.8 nm. It is calculated with a simple effective mass approach ($m = 0.027\ m_0$). The confining potential is $V = 630$ meV. The dashed lines represent only the first state (energy level) for each IR A1, B2, B1 and A2. Additional B2 energy levels (2B2, 3B2, 4B2 . . .) are located between 1B2 and 1B1 energy levels but are not represented. (b) The electronic spectrum for an elliptic InAs/InP QD with thickness 4 nm, and long and short axes 45 and 35 nm. It is calculated with a simple effective mass approach ($m = 0.027\ m_0$). The confining potential is $V = 460$ meV. The dashed lines represent only the first state (energy level) for each IR A1, B2, B1 and A2.

mass and confining potential for electrons in the conduction band were chosen to be equal to $m = 0.027\ m_0$ and $V = 630$ meV respectively. According to our model, the eccentricity of the confined domain is equal to 0.993. The values of 17.8 and 150 nm of the dimensions along the principal axes A and B of the ellipse were kept constant for our calculations. The first confined states energies for the A1, B1, A2, B2 IRs are respectively 384, 474, 485 and 390 meV (see figure 10(a)). The 1A1 state is the ground state. According to the selection rules for intersubband transitions (see section 3.7) the transitions may be observed either between 1A1 and 1B1 states along the $[1\bar{1}0]$ direction or between 1A1 and 1B2 states along the [110] direction. The transition energy for the $[1\bar{1}0]$ direction is then calculated to be equal to 90 meV, in good agreement with the experimental value of 96 meV [11]. The transition energy along the [110] direction is too small (6 meV) to be directly measured with the photoinduced mid-infrared absorption technique [11].

4.3. The application to self-organized InAs QDs on InP substrate

The electronic intersubband transitions were determined experimentally for InAs QDs grown on InP substrate [37, 38]. The experimental transition energies between the states along the $[1\bar{1}0]$ and [110] directions are respectively equal to 35 and 60 meV [37]. Geometrical parameters were estimated only from atomic force microscopy (AFM) measurements and not TEM measurements as in [11]. The lateral dimensions of the base plane were estimated to about 45 and 35 nm respectively along the directions $[1\bar{1}0]$ and [110] (the eccentricity is equal to 0.63). The height is estimated to about 4 nm [37]. For the calculations, we have chosen the same mass ($0.027\ m_0$) as in section 4.2. A smaller confining potential in the conduction band ($V = 460$ meV) is used because the buffer is InP instead of InAlAs. The

first confined states energies for the A1, B1, A2, B2 IRs are respectively 248, 283, 315 and 272 meV (see figure 10(b)). The simulated transition energies between the states along the directions $[1\bar{1}0]$ and [110] are respectively equal to 24 and 35 meV. These values are smaller than the experimental ones. This seems to indicate that the average lateral dimensions of the QDs are significantly smaller than the lateral dimensions of the base. This is indeed what is discussed in [29]. The QDs could be bounded laterally by {111}B facets. Other authors have measured facet inclinations equal to 18°–22° or 45° for InAs/InP islands with similar base dimensions [36, 39]. Transition energies between the states along the directions $[1\bar{1}0]$ and [110] were recalculated by decreasing the lateral dimensions. Calculated values close to the experimental results 35 and 60 meV [36] are then obtained for smaller average lateral dimensions equal to 35 and 24 nm. For this case, the eccentricity is larger and equal to 0.73. These calculations show that it is possible to obtain a reasonable correlation between experimental and calculated values using a few geometrical parameters.

5. Conclusion

The problem of quantum-confined heterostructures is studied with elliptic cylindrical coordinates and a basis of symmetry-adapted Mathieu functions. The conventional effective mass Hamiltonian is derived in 2D and 3D cases (QW and QD). By considering the form of the Hamiltonian, it is shown that the problem does not separate into an internal and an external domain as shown in [15]. A variational method based on a basis of Mathieu functions adapted to the geometrical symmetry of the problem is proposed. Using symmetry considerations and numerical computations of the wavefunction expansions, energy splittings, optical intersubband and interband transition spectra are analysed. Polarization effects for intersubband optical transitions are predicted. Finally the variational method is extended to a 3D problem and applied to the case of self-organized InAs/InAlAs and InAs QDs on InP substrate. Shape-adapted parameters such as the average diameter and the eccentricity are emphasized because they may provide a first simple description of the QD geometry in relation to the available experimental data. This approach is clearly less sophisticated than recent theoretical approaches, where one can arrive at a consistent picture of both the material and the electronic structure by interactive iteration between theory and experiment [42]. However, in this last case, the theoretical approach is much more complicated, and precise experimental information about the size, shape, composition profiles and optical properties of the quantum islands are available. This is not the case up to now for InAs islands grown on InP substrates.

References

[1] Grundmann M, Bimberg D and Ledentsov N N 1998 *Quantum Dot Heterostructures* (Chichester: Wiley)
[2] Sugawara M 1999 *Self-Assembled InGaAs/GaAs Quantum Dots, Semiconductors and semimetals, 60* (New York: Academic)
[3] Alferov Zh I 1998 Quantum wires and dots show the way forward, III-Vs *Review* **11** 47–52
[4] Stier O, Grundmann M and Bimberg D 1999 *Phys. Rev.* B **59** 5688
[5] Pryor C 1999 *Phys. Rev.* B **60** 2869
[6] Sercel P C and Vahala K J 1990 *Phys. Rev.* B **42** 3690
[7] Marzin J Y and Bastard G 1994 *Solid State Commun.* **92** 437
[8] Vasanelli A, De Giorgi M, Ferreira R, Cingolani R and Bastard G 2001 *Physica* E **11** 41
[9] Vasanelli A, De Giorgi M, Ferreira R, Cingolani R, Sakaki H and Bastard G 2001 *Japan. J. Appl. Phys.* **40** 1955
[10] Miska P, Paranthoen C, Even J, Bertru N, Lecorre A and Dehaese O 2002 *J. Phys.: Condens. Matter* **14** 1
[11] Péronne E, Pollack T, Lampin J F, Fossard F, Julien F, Brault J, Gendry G, Marty O and Alexandrou A 2001 *Phys. Rev.* **63** 081307
[12] Cantele G, Ninno D and Iadonisi G 2000 *J. Phys.: Condens. Matter* **12** 9019

[13] Cantele G, Piacente G, Ninno D and Iadonisi 2002 *Phys. Rev.* B **66** 113308
[14] Van den Broeck M and Peeters F M 2001 *Physica* E **11** 345
[15] Lew Yan Voon L C, Galariu C and Willatzen M 2003 *Physica* E **18** 547
[16] Arfken G 1966 *Mathematical Method for Physicists* (New York: Academic)
[17] Mathieu E 1868 *J. Math. Pure Appl.* **13** 137
[18] Morse P M and Feshbach H 1953 *Methods of Theoretical Physics* (New York: McGraw-Hill)
[19] McLachlan N W 1951 *Theory and Applications of Mathieu Functions* (London: Oxford University Press)
[20] Abramovitz M and Stegun I A 1972 *Handbook of Mathematical Functions* (New York: Dover)
[21] Byun W J, Yu J W and Myung N H 1998 *IEEE Trans. Microw. Theory Tech.* **46** 1336
[22] Gutierrez-Vega J C, Iturbe-Castillo M D and Chavez-Cerda S 2000 *Opt. Lett.* **25** 1493
[23] Mongiardo M 1999 *IEEE Trans. Microw. Theory Tech.* **47** 2473
[24] Gutierrez-Vega J C, Chavez-Cerda S and Rodriguez-Dagnino R 1999 *Rev. Mex. Fis.* **45** 613
[25] Ancey S, Folacci A and Gabrielli P 2001 *J. Phys. A: Math. Gen.* **34** 1341
[26] Saito H, Nishi K and Sugou S 2001 *Appl. Phys. Lett.* **78** 267
[27] Wang R H, Stinz A, Varangis P M, Newell T C, Li H, Malloy K J and Lester L F 2001 *IEEE Photonics Technol. Lett.* **13** 767
[28] Paranthoen C, Bertru N, Lambert B, Dehaese O, Le Corre A, Even J, Loualiche S, Lissillour F, Moreau G and Simon J C 2002 *Semicond. Sci. Technol.* **17** L5
[29] Ni Allen C, Poole P J, Marshall P, Fraser J, Raymond S and Fafard S 2002 *Appl. Phys. Lett.* **80** 3629
[30] Paranthoen C, Platz C, Moreau G, Bertru N, Dehaese O, Le Corre A, Miska P, Even J, Folliot H, Labbé C, Patriarche G, Simon J C and Loualiche S 2003 *J. Cryst. Growth* **251** 230
[31] Saito H, Nishi K, Kamei A and Sugou S 2000 *IEEE Photonics Technol. Lett.* **12** 1298
[32] Saito H, Nishi K and Sugou S 2001 *Electron. Lett.* **37** 1293
[33] Bastard G 1992 *Wave Mechanics Applied to Semiconductor Heterostructures* (Paris: EDP)
[34] Le Goff S and Stébé B 1993 *Phys. Rev.* B **47** 1383
[35] Paranthoen C, Bertru N, Platz C, Caroff P, Dehaese O, Folliot H, Le Corre A and Loualiche S 2003 *J. Cryst. Growth* **257** 104
[36] Ponchet A, Le Corre A, L'Haridon H, Lambert B, Salaun S, Groenen J and Carles R 1996 *Solid State Electron.* **40** 615
[37] Pettersson H, Warburton R J, Kotthaus J P, Carlsson N, Seifert W, Pistol M E and Samuelson L 1999 *Phys. Rev. Rapid Commun.* B **60** R11289
[38] Carlsson N, Junno T, Montelius L, Pistol M E, Samuelson L and Seifert W 1998 *J. Cryst. Growth* **191** 347
[39] Frechengues S, Bertru N, Drouot V, Lambert B, Robinet S, Loualiche S, Lacombe D and Ponchet A 1999 *Appl. Phys. Lett.* **74** 3356
[40] Oksanen J and Tulkki J 2003 *J. Appl. Phys.* **94** 1983
[41] Miska P, Paranthoen C, Even J, Dehaese O, Folliot H, Bertru N, Loualiche S, Senes M and Marie X 2002 *Semicond. Sci. Technol.* **17** L63
[42] Shumway J, Williamson A, Zunger A, Passaseo A, DeGiorgi M, Cingolani R, Catalano M and Crozier P 2001 *Phys. Rev.* B **64** 125302